Impact of point defects on the electrical properties of selenium: A density functional theory investigation with discussion of the entropic term

Adrien Stoliaroff, Camille Latouche ⬤, and Stéphane Jobic[*]
Université de Nantes, CNRS, Institut des Matériaux Jean Rouxel, IMN, F-44000 Nantes, France

Selenium in ambient conditions exhibits two crystalline allotropic forms. The thermodynamically stable phase is the pseudo-1D trigonal form with $^1/_\infty$[Se] chains. A metastable phase composed of [Se_8] rings also coexists. Both are studied herein by means of density functional theory. The recent SCAN functional offers a fair description of both phases. The Birch-Murnaghan equation of states is fitted onto *ab initio* results to obtain the energy-volume and pressure-energy relationships. Phonon properties (bands and DOS) are computed and a pressure-temperature phase diagram is derived. Intrinsic and extrinsic defect formation enthalpies are also computed using SCAN functional and HSE06-GD3 for the band shifts. The low *p*-type conductivity of the trigonal phase can be attributed to Se self-interstitials while the very low conductivity of the metastable phase is related to very deep native defects. Antimony, and bromine extrinsic defects are tested as potential dopants. Of those three, only antimony in the trigonal phase seems to possibly have a positive impact on the conductivity. Finally, the configurational entropy linked to defect creation is computed. Our calculations clearly show that the usual assumption that defect entropy is negligible compared to the enthalpy seems relevant.

I. INTRODUCTION

Elemental selenium has recently regained attention for its optoelectronic properties [1]. In particular, selenium is of historical interest as photoconductivity was first noticed in this material in 1873 [2], leading to the first PV solar cells with an efficiency lower than 1% [3]. It was improved to culminate in 1985 at the record efficiency of 5.0% [4]. Its high band gap and the parallel development and success of the silicon industry resulted in it being set aside for PV application. However, it was very recently pointed out that the material could provide a convenient absorber for the top cell of a tandem solar cell [1]. Indeed, synthesizing a unary material is much easier than ternary or quaternary materials now used in thin-film technologies such as copper-indium-gallium-selenide (CIGS) and copper-zinc-tin-selenide (CZTS). In this vein, Todorov *et al.* recently optimized a selenium-based single-junction device and broke the previous record, reaching 6.5% efficiency [1]. In this cell, crystallized *p*-type selenium acts as an absorber layer. Todorov *et al.* note that the open-circuit voltage (V_{OC}) is almost 1 V under the theoretical Shockley-Queisser limit, leaving much room for improvement, especially through the limitation of charge carriers recombinations. This issue is typically linked to point defects, both in the bulk and/or at the heterojunction [5]. This brand new record translates the recent research activity around the application of selenium for solar devices, be it as an absorber for photoelectrochemical solar cells [6] and PV cells in thin films [7], as nanoparticles [8], or as a hole conducting layer [9,10]. More generally, the nanoscale forms have also attracted a fair deal of interest,

partly due to its potential application in the fields of medicine and optical devices [11,12].

Looking at the material itself in more detail, the phase diagram is quite complex, with the coexistence of several allotropic forms due to the competition between short range covalent bonds and long range van der Waals interactions [13,14]. Parthasarathy and Holzapfel experimentally reported a structural study up to 50 GPa [15], later completed by Akahama *et al.* up to 140 GPa [16]. The first pressure-induced transition occurs at *ca.* 14 GPa. Intermediate structures are unclear, but the material adopts a monoclinic lattice between *ca.* 23 and *ca.* 28 GPa. At higher pressures, a rhombohedral phase isostructural to β-polonium appears, and at 140 GPa an additional structural transition towards a body-centered cubic (BCC) phase occurs. The highest pressure phases have been more thoroughly studied, most notably for supraconducting properties [16–19]. Ambient conditions are of most interest for the optoelectronic applications on which this work focuses. In such conditions, the material can adopt three different forms, namely an amorphous form and two crystalline ones. The first crystal phase, hereafter referred to as γ-Se, crystallizes in a trigonal lattice, exhibiting a band gap of 1.83 eV [20] or 2 eV [21] according to the authors. This is without a doubt the most stable phase of selenium at ambient pressure [14,22], and it is often incorrectly referred to as "hexagonal" selenium in the literature. The crystallographic structure is described in more details hereafter. The second crystal form obtained in ambient conditions adopts a monoclinic lattice and is labelled herein β-Se [23,24]. Its band gap is reported as direct and is equal to 2.53 eV [25].

The purpose of this work is to determine the intrinsic defects present in the two main crystal forms of selenium in order to identify the origin of the observed *p*-type

_____

[*]stephane.jobic@cnrs-imn.fr

TABLE I. Computational details of the study of ideal cells.

	β-Se (rings)	γ-Se (chains)
	General	
E_{cut} (eV)	265	
Force conv. (eV Å^{-1})	10^{-2}	
SCF conv. (optim.) (eV)	10^{-5}	
SCF conv. (DOS) (eV)	10^{-6}	
PBE/PBE-GD3(BJ)/SCAN(-GD3)		
K-pts grid (optim.)	MP 5×5×4	MP 10×10×8
K-pts grid (DOS)	Γ 5×5×4	Γ 15×15×12
HSE06(-GD3)		
K-pts grid (optim.)	Γ 2×2×2	MP 5 × 5 × 4
K-pts grid (DOS)	Γ 3×3×3	Γ 5×5×4

conductivity. Extrinsic doping strategies are also investigated. Finally, advantage is taken from the relative simplicity of the system to discuss the entropic contribution to the Gibbs' free energy and validate the common hypothesis that it is negligible.

II. COMPUTATIONAL DETAILS

A. Ground state of the ideal systems

Computations were performed using the plane-augmented waves (PAW) scheme implemented in VASP [26–29]. Several approximations were tested, namely "pure" GGA functional PBE [30], including dispersion corrections GD3 [31,32] and GD3-BJ [31–33] to account for long range interactions, meta-GGA functional SCAN [34] both without and with GD3 energy correction [31,32], and screened hybrid functional HSE06 [35,36] and HSE06-GD3. The calculation settings (K-mesh, energy cutoff, convergence criteria) for the geometrical optimization and DOS for the two phases studied are summarized in Table I.

B. Pressure and temperature effects

To take into account the effect of pressure, a series of six additional cells with different $\frac{V}{V_0}$ ratios were built from the relaxed structure of volume V_0 at $P = 0$ (PBE-GD3-BJ for β-Se and PBE-GD3 for γ-Se). They were optimized at constant volume. The values (cell parameters and interatomic distances) show that these functionals can be satisfactorily

used for such purpose [37]. The $E(V)$ data was fitted using the Birch-Murnaghan equation of state as implemented in PyDEF [37–39].

Density functional perturbation theory (DFPT) [40] could not be used to calculate the phonon properties because the dispersion corrections are not included in the Hessian matrix in VASP 5.4.4. Thus, the finite-displacement method was used with 2×2×2 supercells. This numerical method might induce minor discrepancies. The related post-treatment was performed using the PHONOPY code [41] used as a library in PyDEF.

C. Defect study

Based on the results presented hereafter, faulted supercells were built on the SCAN geometry. The cutoff energy was increased to 500 eV due to the study of extrinsic defects. The computational details are summarized in Table II. Defect formation enthalpies ΔH at $T = 0$ and $P = 0$ with respect to Fermi level μ_{E_F} were computed following equation (1).

$$\Delta H_{form}^{D,q}(\mu_{E_F}) = E_{total}^{D,q} - E_{total}^{host} + \sum_{X_i} n_{X_i}\left(\mu_{X_i}^0 + \Delta\mu_{X_i}\right)$$
$$+ q\left(E_{VBM}^{host} + \mu_{E_F}\right) + corr(D, q), \qquad (1)$$

where

(i) $E_{total}^{D,q}$ is the total energy of the faulted supercell (the supercell containing the defect) after relaxation of the atomic positions at fixed cell parameters without symmetry constrains.

(ii) E_{total}^{host} is the total energy of the ideal supercell (also referred to as the host cell).

(iii) $\mu_{X_i}^0$ is the chemical potential of element X_i in its standard phase (ambient conditions).

(iv) $\Delta\mu_{X_i}$ is the variation of the chemical potential of element X_i from its chemical potential in the thermodynamic standard phase ($\Delta\mu_{X_i} < 0$), induced by the crystal growth conditions.

(v) n_{X_i} is the number of atoms of species X_i added to the ideal host lattice.

(vi) E_{VBM}^{host} is the energy corresponding to the valence band maximum (VBM). It is the reference energy for μ_{E_F}.

(vii) μ_{E_F} is the chemical potential of the electrons, the so-called Fermi level.

(viii) $corr(D, q)$ corresponds to various corrections to take into account and detailed in the Supplemental Material.

TABLE II. Computational details for the defect study.

	β-Se (rings)		γ-Se (chains)
	General		
E_{cut} (eV)		500	
Force conv. (eV Å^{-1})		10^{-2}	
SCF conv. (optim.) (eV)		10^{-5}	
SCF conv. (DOS) (eV)		10^{-6}	
Electronic density functional		SCAN	
Supercell	2×2×1 (128 atoms)		3×3×3 (81 atoms)
K-points grid (optim.)	MP 2×2×2		MP 3×3×3
K-points grid (DOS)	Γ-centered 2×2×2		Γ-centered 5×5×4

Band shift, as well as potential alignment, electrostatic Makov-Payne-like, Moss-Burstein band filling and perturbed host states (PHS) total energy corrections were taken into account as in our previous works [42,43]. The band-edge references were taken from HSE06-GD3 calculations. The post-treatments were performed using our in-house software PyDEF [38,39].

III. RESULTS AND DISCUSSION

A. Ground state properties of the two allotropic ambient crystal phases

As mentioned beforehand, selenium in solid state can adopt several allotropic forms. The crystallographic structures of the two main crystal phases β-Se and γ-Se are drawn in Figs. 1 and 2 [37]. The first crystallizes in a monoclinic lattice following space group symmetry $P2_1/c$ (no. 14), forming Se_8 crownlike rings. It is isostructural to α-S_8. The rings roughly
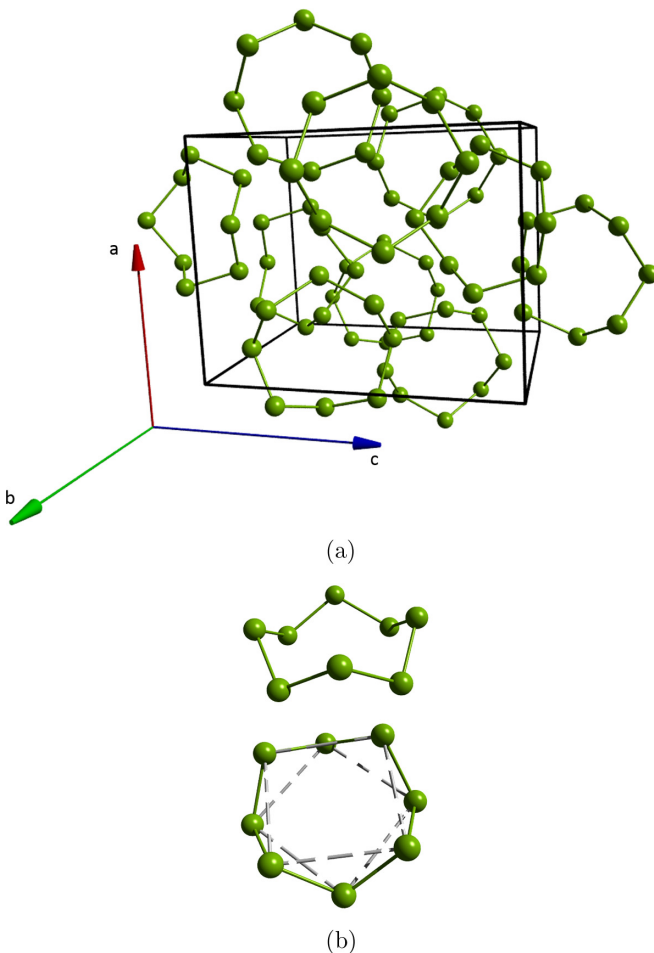
FIG. 1. Crystallographic structure of β-Se, exhibiting a monoclinic lattice within $P2_1/c$ (no. 14) space group symmetry. It is isostructural to α-S_8. Green spheres represent selenium atoms. (a) Conventional cell. Cell boundaries are represented in black. (b) One isolated crown-shaped Se_8 ring moiety. Plain green lines represent chemical bonds and dotted gray ones draw the two squares of four Se atoms composing the crown. $a = 8.894$ Å, $b = 9.000$ Å, $c = 11.383$ Å, $\alpha = \gamma = 90°$, $\beta = 90.68°$ [24].
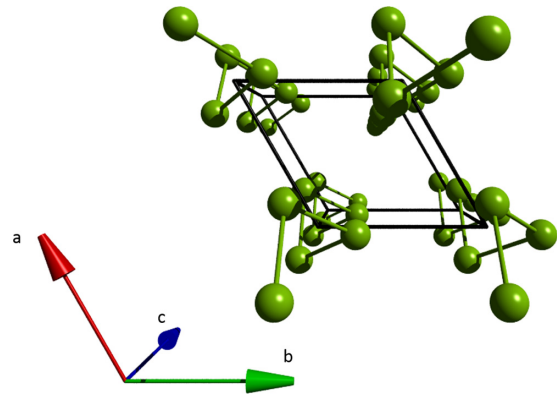
FIG. 2. Crystallographic structure of γ-Se (conventional cell). The structure is often inaccurately referred to as "hexagonal" Se but it crystallizes in a trigonal lattice, within $P3_121$ (no. 152) space group symmetry. It consists of $^1/_\infty$ [Se] helical chains along the c axis. $a = b = 4.368$ Å, $c = 4.958$ Å [48].

consist of two (almost) parallel squares of four Se atoms shifted by $45°$ [22]. The conventional cell contains four Se_8 rings for a total of 32 atoms. As of γ-Se, the conventional cell is highly anisotropic with infinite helical chains of bicoordinated Se along the c axis of a trigonal lattice ($P3_121$ space group, no. 152). Subsequently, the conventional cell contains three (crystallographically equivalent) atoms. The amorphous form, noted a-Se, might be apprehended as a mixture of the two moieties, chains and Se_8 rings, or a glass of either one. However, no structural model could be determined with certainty for a-Se and the amorphous structure may well vary with the synthesis process [44–46], although a recent nuclear magnetic resonance (NMR) spectroscopy study by Marple *et al.* suggests that their samples of a-Se contained only $^1/_\infty$ [Se] chains [47]. Hereafter, only the two β- and γ-Se forms are discussed.

The two structures present voids (van der Waals gaps) between the chemical entities (Se_8 rings or infinite chains), a clue of the importance of weak interactions to maintain the cohesion of the microscopic organization of matter. Computed geometric parameters are reported in Supplemental Material [37]. Let us start the analysis of the ability of the different functionals to reproduce a correct geometry with β-Se. The large overestimation of the b and c lattice parameters using PBE and HSE06, and also corrected by the use of dispersion schemes GD3 and GD3-BJ, demonstrates the importance of weak interactions in the structure. Within the GGA approximation, PBE-GD3-BJ outperforms PBE and PBE-GD3 in terms of structural description. The overall good prediction of nearest-neighbor distances with poor cell parameters and van der Waals distance predictions for the uncorrected functionals means that each moiety (chain or ring) is correctly reproduced. However the different entities are too far apart from one another, i.e., the size of the van der Waals gap is overestimated. This can be explained by the fact that DFT functionals account well for short-range interactions but not long-range ones.

The computational effort required for a hybrid functional calculation being very heavy, it is important to consider reliable and efficient protocols. The SCAN functional, which

gains in popularity among computationally-oriented material scientists [49], was tested here. Interestingly, uncorrected SCAN leads straight away to a relatively satisfying optimized geometry for β-Se, with a maximum relative deviation towards experimental cell parameters of 3.50%. The agreement with experiment is still improved with the addition of the GD3 scheme. To summarize, when considering the minimization of cell parameters deviation between simulation and experiment for β-Se, PBE-GD3-BJ, SCAN, and HS06-GD3 give similarly satisfying results with a $\simeq 3\%$ maximum deviation in absolute value and SCAN-GD3 an even closer description.

Before discussing the band-gap values, let us investigate the γ-Se 1D structure. Once more, HSE06 severely overestimates the $a = b$ parameter due to weak interactions. Surprisingly, PBE does not have such a problem. The cell parameters decrease when adding dispersion schemes GD3 and GD3-BJ as expected. The GD3-BJ correction to PBE is inappropriate in the case of γ-Se, shrinking $a = b$ too much leading to a 7% underestimation with respect to experiment. The long range interactions seem less strong than in the β-Se case. The trend is the same at the meta-GGA level with SCAN-GD3 underestimating $a = b$ by 3.4% against a slight overestimation of 1.7% by SCAN. Overall the c parameter, i.e., the spatial period along the chain direction, is satisfyingly described with all methods. The closest geometry to experiment is the one calculated with HSE06-GD3 with less than one percent deviation in absolute value.

The electronic band structure of both β- and γ-Se forms computed with the SCAN functional are reported in Supplemental Material [37]. Both compounds are semiconductors. The gap values are discussed more in details hereafter, however it should be mentioned here that the existence of an electronic gap is preserved with all the functionals tested, even uncorrected GGA-PBE. β-Se (rings) exhibits a direct band gap of 1.74 eV on the $\Gamma - Y$ segment while γ-Se shows an indirect $L - H$ band gap of 1.29 eV. The electronic bands of β-Se are quite flat, which translates as high charge carrier effective masses and low mobility. This can be understood as the electronic states are localized onto a Se_8 ring and the inter-ring interaction is weak and of van der Waals nature. The flatness of the bands is correlated to the pseudo-0D character of the structure which exhibits separate moieties. On the contrary, the dispersion of the electronic bands of γ-Se is much more important due to its pseudo-1D structure.

The most substantial modification of the band diagram when changing the approximation for the electronic exchange correlation is the increase in the gap when climbing Jacob's ladder of *ab initio* simulations. Now the quality of the gap simulation is discussed with respect to the choice of functional. The experimental and computed DOS gap values are reported in Table III.

The well-known band-gap problem at the GGA level is visible with a band-gap underestimation of $\simeq 40\%$ for β-Se and 50% for γ-Se. In the case of the GGA description of β-Se, it means that the closer to experiment the cell parameters are, the more underestimated the band gap is. At the meta-GGA level, pure SCAN is in both cases closer to the experimental value than SCAN-GD3 but the gap remains underestimated by $\simeq 30\%$. Going from GGA to meta-GGA is not sufficient to get a band gap very close to the experimental value but

TABLE III. β- and γ-Se electronic DOS band gap (eV) calculated using different methodologies compared with experimental data.

	β-Se (rings)	γ-Se (chains)
Exp.	2.53 [25]	1.83–2.00 (1.91) [20,21,50]
PBE	1.55 (−39%)	0.96 (−50%)
PBE-GD3	1.29 (−49%)	0.57 (−70%)
PBE-GD3-BJ	1.07 (−58%)	0.45 (−76%)
SCAN	1.75 (−31%)	1.32 (−31%)
SCAN-GD3	1.62 (−36%)	1.00 (−48%)
HSE06	2.75 (9%)	2.58 (35%)
HSE06-GD3	2.33 (−8%)	2.02 (6%)

provides a fair improvement at negligible computational cost. The HSE06 geometries being very distorted compared to the experimental ones, they will not provide suitable models for these materials, even if the band gap can be (perhaps by coincidence) quite close to the experimental one, as is the case for β-Se. The HSE06-GD3 gap simulation is quite good with an 8% underestimation in the case of β-Se and 6% overestimation in that of the γ-phase. The introduction of 25% of Hartree-Fock exchange allows us to recover the gap, along with a structure closer to experiment thanks to the GD3 scheme.

HSE06-GD3 provides the most reliable structural and electronic description combined for both compounds and is thus retained as the reference calculation to position the band edges in the latter defect study. However, relaxing the faulted supercells at this level of approximation would be too cumbersome and a less demanding functional is required for the defect study. SCAN provides a convenient way to describe reliably both compounds using state-of-the-art functional of affordable computational cost, thus is retained for the defect study.

B. Defect formation enthalpies

Then, point defects are investigated in both β and γ phase in order to understand the origin of the p-type conductivity of the materials and explore potential dopants which may prove useful for their application in optical devices. The SCAN functional is used throughout the defect study as mentioned previously. Note that in addition to the SCAN lattice parameters being in good agreement with the experimental ones, the interatomic distances are also very well reproduced, with a deviation with respect to experiment inferior to 3%. As summarized in Table II, a $2\times2\times1$, $3\times3\times3$ supercell is used for β-, γ-Se, respectively.

Computational studies allow us to screen the periodic table for dopants in an affordable and efficient way, prior to experiment in order to give valuable insights to guide synthesis. In that spirit, the following extrinsic defects were also considered. Following the same line of thoughts as aliovalent doping in Si, any V (VII) element substitution to Se should induce p-type (n-type) doping. Due to prior investigation of Sb_2Se_3, Sb was selected over P and As. Bromine was considered for electron doping.

TABLE IV. Chemical potential values in electronvolts, as computed with the SCAN functional. $\Delta\mu$, i.e., the variation from standard chemical potential, is indicated in brackets. μ_{Br}^0 was not computed as bromine is liquid in standard conditions. The competing binary phase limiting the stability domain of the selenium phase (β-Se ringlike and γ-Se chainlike structures) is indicated with a slash in the left column.

	β-Se	γ-Se
μ_{Se} ($\Delta\mu_{Se}$)	-20.076 ($+0.009$)	-20.085 (0.000)
μ_{Sb} ($\Delta\mu_{Sb}$) /Sb$_2$Se$_3$	-37.873 (-0.610)	-37.860 (-0.597)
μ_{Br} ($\Delta\mu_{Br}$) /SeBr$_4$	-19.548 ($-$)	-19.546 ($-$)

β- and γ-Se are unary compounds, so the chemical potential of selenium is taken as the energy per atom, and only one synthesis condition is represented in the intrinsic defect model. The difference in selenium chemical potential between the two phases is small (9.0 meV), highlighting the fact that the two coexist at ambient temperature and pressure. The chemical potential values are available in Table IV.

Only the total energy of one binary needs to be computed for each dopant considered in order to obtain the maximum possible dopant chemical potential value. The obtained value corresponds to the total chemical potential μ_X which can be expressed as $\mu_X = \mu_X^0 + \Delta\mu_X$ as employed in equation (1). The binary compound with the lowest dopant content will set this limit. Thus, Sb$_2$Se$_3$ (*Pnma*, no. 62) and SeBr$_4$ (*P31c*, no. 159) were considered for antimony and bromine, respectively.

In this unary compound, only two types of intrinsic defects can be considered, namely vacancies and interstitials. β-Se exhibits eight distinct crystallographic sites, all of them being very similar in terms of environment (bicoordinated). As our previous work has shown that the environment is the driving force for important vacancy DFE difference, only one vacancy was considered in β-Se. The structure of γ-Se offers only one crystallographic position, so there is no ambiguity on the vacancy position. A Frenkel defect (Se$_i$ + V$_{Se}$) was build for the γ phase but could not be stabilized. This relaxation leads the displaced atom back to its initial position within the ideal arrangement.

Let us examine the DFE of the intrinsic defects, as reported in Fig. 3. In both cases, V$_{Se}$ is lower in enthalpy than Se$_i$ in the *p*-type regions, and both defects exhibit quite a low enthalpy of formations, inferior to 2 eV. However, the negative *U* behavior of the chalcogen vacancy is found only in the γ phase. The formation enthalpies of the nonzero charge states are too high for the transition levels $+2/+1$ in β- and $+1/0$ in γ-Se to be above the VBM with $\epsilon_{+2/+1}^{\beta} \simeq \epsilon_{+1/0}^{\gamma} = -0.12$ eV. The $\epsilon_{+1/0}^{\beta}$ transition level is located 0.035 eV below the VBM, i.e., 2.28 eV under the CBM. Consequently, V$_{Se}$ is totally unable to give any electron to the CB. Both positive and negative defect charges were computed in order to account for all possible effects in these unary compounds. The less expected ones, i.e., negative for the vacancy and positive for the interstitial, were found to play no role in the defect physics of these compounds.

The energetic cost associated with the creation of a selenium vacancy in the two phases is quite different. For the

(a)

(b)
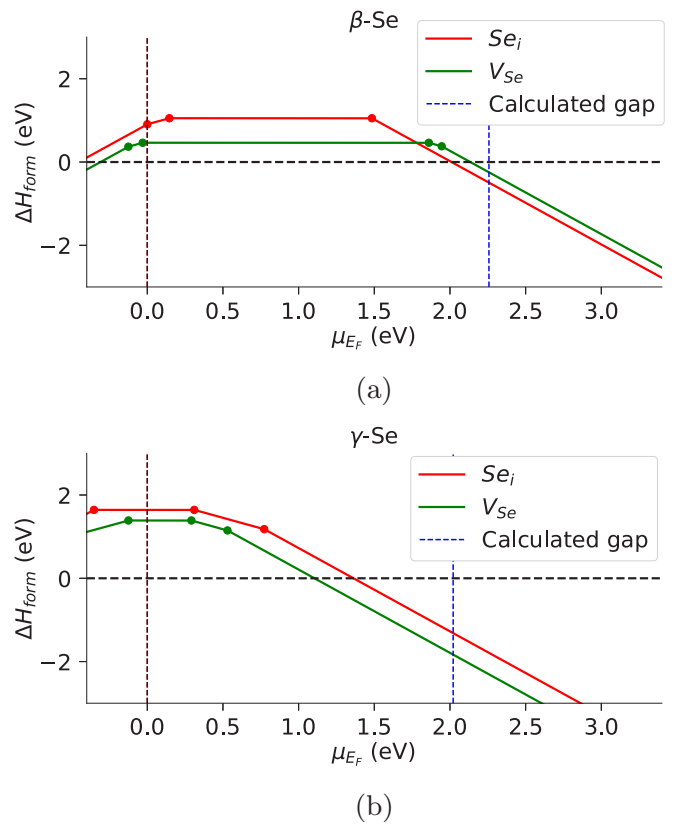
FIG. 3. DFE of intrinsic defects plotted against Fermi level μ_{E_F} (a) in β-Se ($E_g = 2.33$ eV) and (b) in γ-Se ($E_g = 2.02$ eV). The vertical black and blue dotted lines stand for the VBM and CBM, respectively. The calculated gap is the HSE06-GD3 band gap.

neutral state of charge, it is of 0.46 eV in β-Se against 1.39 eV in γ-Se. Counterintuitively, it cannot be directly related to the bond lengths. Indeed, the Se-Se interatomic distance is 2.345 Å (2.335–2.358 Å) in β-Se, 1.4% shorter than 2.378 Å in γ-Se. The strength of the chemical bond is expected to increase when the interatomic distance decreases. The comparison between perfect and faulted geometries represented in the Supplemental Material provides an interesting insight into the reason for the DFE difference for V$_{Se}$ between the two allotropic forms [37]. The relaxation of the structures after the vacancy formation occurred leads to two very distinct situations. In β-Se, once the two chemical bonds are broken by the formation of the vacancy, the structure is able to recover a ring shape after relaxation. On the other hand, in γ-Se the infinite chain is broken. One covalent bond is replaced by a long range interaction. Thus, Se$_1$ in γ-Se in the final configuration exhibits a radical change in environment. This explains why, in spite of *a priori* stronger Se-Se bonds in β-Se, it is easier to create a vacancy in β- than in γ-Se. As the γ-Se phase is very anisotropic and periodic boundary conditions are applied, the DFE of V$_{Se}$ was validated against another supercell (2×2×7) to ensure the quality of the result.

The behavior of Se$_i$ however is very different between the two phases. In β-Se, the $0/-2$ transition level stands far above the VBM at 1.48 eV, whereas in γ-Se $\epsilon_{0/-1}$ exists and is located only 0.31 eV above it. $\epsilon_{-1/-2}$ sits 0.77 eV above the VBM. Thus, the self-interstitial is expected not to contribute

TABLE V. Fermi level (eV) at growth temperature (K) and after quenching at room temperature (300 K), calculated free hole and electron concentrations at room temperature, and intrinsic defect concentrations (cm^{-3}) in γ-Se with respect to growth temperature.

T_{growth}	E_F^{gr}	E_F^{room}	n_h	n_e	$[V_{\text{Se}}]$	$[\text{Se}_i]$
500	0.66	0.37	$1.0.10^9$	$1.6.10^{-12}$	$3.6.10^8$	$1.0.10^9$
800	0.49	0.15	$7.3.10^{12}$	$2.3.10^{-16}$	$6.3.10^{13}$	$7.3.10^{12}$
1000	0.38	0.07	$1.5.10^{14}$	$1.1.10^{-17}$	$3.5.10^{15}$	$1.5.10^{14}$

to free carriers concentrations in the ring form while being a fair acceptor defect in the linear allotropic form. The DFE also varies significantly from one structure to the other. While the DFE of Se$_i$ in the neutral state of charge is 1.1 eV in β-Se, it is 1.64 eV in γ-Se, roughly 0.5 eV higher. It is very clear that the ring structure is far more prone to intrinsic defects than the linear one. However, the concentrated defects of β-Se are very deep defects and do not give rise to free charge carriers, while Se$_i$ in γ-Se is a fair acceptor.

Although the Fermi level μ_{E_F} is often taken as a variable, it is important to keep in mind that for an isolated material, the charge neutrality imposes one single possible value for the Fermi level at a considered growth temperature. The effective masses of the charge carriers are obtained by fitting a parabolic model onto the band extrema. For β-Se, a difficulty emerges. The N^{sites} prefactor in the expression of the defect concentration, as written in equation (2), is the number of available sites for the defect.

$$n_D = N_D^{\text{sites}} \left(e^{\frac{-\Delta H_{\text{form}}^{D,q(E_F^{gr})}(E_F^{gr})}{k_B T_{gr}}} \right) \qquad (2)$$

Although its value is obvious in the case of vacancies, it is much more ambiguous in the case of an interstitial in β-Se for two reasons discussed hereafter. In many materials, unoccupied crystallographic sites provide potential host sites for interstitials which are both obvious to the physico-chemist's eye and prove significantly lower (several tenth of electron-volts) in energy than other potential interstitial sites in DFT calculations. In β-Se, due to the flexibility of the structure which results in a very soft/flat potential energy surface, the energy difference between different interstitial sites is much lower, making it harder to discriminate between sites.

For interstitial selenium atoms in γ-Se, N_D^{sites} was considered equal to one per conventional cell ($N = 27$ for the $3\times3\times3$ supercell), a value which seems realistic. This allows the determination of the Fermi level at growth temperature and after quenching at room temperature, as well as the defect concentrations. The simulation results are summarized in Table V. The Fermi level during crystal growth is one third of the band gap above the VBM, near the crossing point of the formation enthalpy curves of the two intrinsic defects (0.66 eV for $T_{\text{growth}} = 500$ K, which corresponds to the synthesis temperature of Todorov *et al.*) [1]. Then, once the defect concentrations are frozen to model a quenching of the material, the Fermi level is dragged down towards the VBM. This is due to the following mechanism. The charge neutrality condition during synthesis imposes the 0.66 eV value for E_F^{growth}. Then the point defect concentrations are

kept constant. Here, the p-type behavior of the material due to the selenium interstitial is reproduced for the Fermi level as well. It highlights the fact that increasing the synthesis temperature will increase the concentration of charge carriers and by extension the conductivity, as the concentration of charged point defects increases with temperature. Note that the maximum hole concentration is quite low (10^{14} cm^{-3} for $T_{\text{growth}} = 1000$ K). This calculated value is in perfect agreement with experimental data [51]. Interestingly, whereas at low synthesis temperature interstitials are more concentrated than vacancies, for growth temperatures above $\simeq$570 K, vacancies become the major defect in pure γ-Se. Defect concentrations are calculated to be inferior to 10^{15} cm^{-3}, comparably to In$_2$S$_3$ [52].

Now that intrinsic defects properties have been thoroughly investigated, the potential dopants mentioned previously are discussed (Sb, Br). The extrinsic DFE curves are reported in Fig. 4. Once more, β-Se proves quite defect tolerant with low (1–2 eV) DFE for all considered defects, except for antimony interstitial. Antimony ($4d^{10}5s^25p^3$) can both exhibit the cationic form Sb^{3+} emptying the $5p$ orbitals as in Sb$_2$Se$_3$ and the anionic form Sb^{3-} saturating the same orbitals, as in AlSb. Thus, six different non-neutral states of charge were considered for Sb$_i$. The transition levels unfortunately are buried deep inside the gap. Bromine can lead to Br_i acceptor and Br_{Se} donor defects. In β-Se, both are deep defects. In γ-Se, the $+1/0$ charge transition level (CTL) of Br_{Se} is located at 0.37 eV, i.e., 1.62 eV below the CBM and is thus very deep. The $0/-1$ CTL of Br_i makes it a good acceptor, however it is more than 0.9 eV higher in formation enthalpy than deep donor Br_{Se}. Br_{Se} is expected to act as a "hole killer" defect as it is much more concentrated than Br_i. To summarize, no efficient dopant for β-Se was found in the list of chemical species we selected. Bromine doping of γ-Se is ineffective with respect to the improvement of the conductivity. Sb$_{\text{Se}}$ in γ-Se is the lowest enthalpy defect in a γ-Se material containing antimony. Its DFE of 1.14 eV in the neutral state of charge, and its $0/-1$ transition level 0.10 eV above the VBM, makes it a far better acceptor defect than the intrinsic Se$_i$.

From those calculations, it can be concluded that the formation of the metastable phase β-Se should be avoided because of its extremely poor conductivity. It appears that Sb doping of γ-Se may be an efficient way to improve the conductivity of selenium layers in optoelectronic devices. The other species tried out, namely bromine, seem irrelevant for such a purpose.

The relative simplicity of the two selenium phases studied (only one chemical species involved) offers the opportunity to try to go beyond the static model at zero temperature. This would allow us to link the simulated variables to experimentally relevant macroscopic quantities, here pressure and temperature. The state function to simulate is no more the enthalpy but the free energy, as discussed hereafter.

IV. FREE ENERGIES

Including the entropy allows us to calculate the free energy $F = E - T \times S$ and considering both pressure/volume effects and temperature to go up to the Gibbs' energy $G = F + PV$ of the system, the thermodynamic quantity which should ideally be evaluated. The relative simplicity of the systems considered
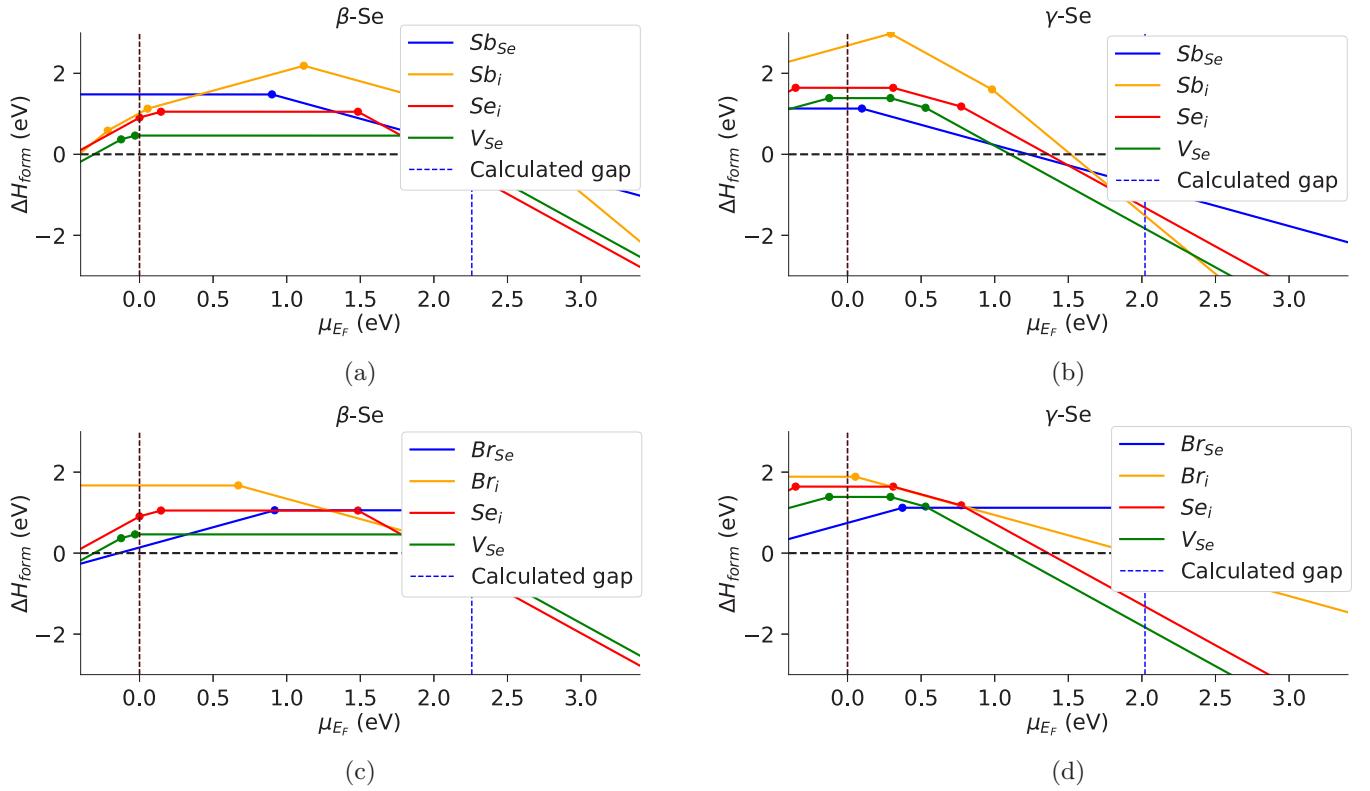
FIG. 4. DFE plotted against Fermi level μ_{E_F} for intrinsic defects and (a) Sb defects in β-Se, (b) Sb defects in γ-Se, (c) Br defects in β-Se, (d) Br defects in γ-Se. ($E_g^\beta = 2.33$ eV and $E_g^\gamma = 2.02$ eV.) The calculated gap is the HSE06-GD3 band gap.

provides the opportunity to check the amplitude of the entropic and volumic terms ignored in the supercell model. The Gibbs' energy for the two ideal structures is calculated first, followed by the free energy of formation of intrinsic defects in γ-Se.

A. Pressure and temperature effects

In order to calculate the Gibbs' energy G for the determination of pressure and temperature dependent phase diagram of crystalline selenium, both pressure and temperature contributions to G, namely $P \times V(P)$ and $T \times S(T)$, must be calculated. It is assumed that at low pressure and temperature, the two variables P and T can be decorrelated so that the two dependencies can be studied separately. The results are then linearly extrapolated to complete the *ab initio* data determined at $P(T = 0)$ and $T(P = 0)$.

To take into account pressure effects, the Birch-Murnaghan equation of states was fitted on a series of energy vs pressure *ab initio* data points [53]. They were obtained by relaxing at constant volume and calculating the energy of compressed/dilated models with PBE-GD3. It was chosen to use the same dispersion scheme for both allotropic forms to enable comparison of the obtained energies. The fit is shown in Fig. 5. The Birch-Murnaghan equation of state has been previously used for high-pressure phases of Se [19]. Young modulus B_0 and its derivative with respect to pressure B_0' are extracted from the fit. B_0 is found to be three times bigger for the β than for the γ phase. As only the total energy from the *ab initio* simulation is extracted to fit the equation of state, PBE-GD3 ought to provide reliable data.

Then, in order to reflect possible temperature effects, phonon properties are investigated within the harmonic approximation. In the ideally ordered structures, the configurational entropy is zero as there is only one possible configuration for the atoms within each structure. The only configuration is the crystallographic arrangement, where all atoms sit at their equilibrium position. Thus, the entropy in the ideal systems only consists of the vibrational entropy. Of course, the situation is fairly different when considering possible crystallographic point defects as will be discussed in the next section. Thus, computing phonon properties of the ideal cells is enough to obtain the entropy of such ordered system. Due to overdelocalization, GGA phonon frequencies are usually underestimated [54].

Phonon band structure and DOS are presented in Fig. 6. The difference in the number of atoms per cell (32 for β-Se and 3 for γ-Se) explains the difference in aspect of the two band structures due to a higher number of bands for β. Vibrational frequencies of the acoustic modes are lower for the β phase (<25 cm^{-1}) than for the γ phase (<80 cm^{-1}). It means that the chemical bond in the chainlike structure is more "rigid" than in the ringlike one. This is coherent with the previous interpretation of β-Se being the most flexible structure of the two. The forbidden frequency gap in the infinite wavelength limit (Γ point) is computed to be 21 cm^{-1} in β-Se and 113 cm^{-1} in γ-Se. The DOS gap between the medium- and high-frequency optical phonons is three times more important for the β than for the γ phase ($\simeq 60$ cm^{-1} vs $\simeq 20$ cm^{-1}). Finally, β-Se exhibits phonon modes of frequencies higher than 250 cm^{-1} while γ-Se does not. All these

(a)

(b)
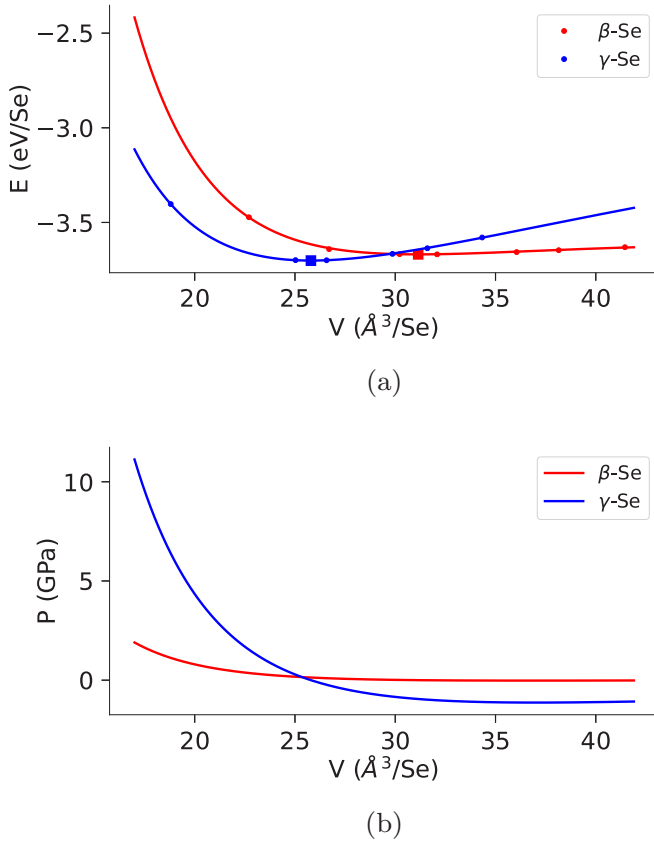
FIG. 5. The Birch-Murnaghan equation of state fitted onto PBE-GD3 calculation series. (a) $E(V)$ curve for β-Se yields $B_0 = 0.16$ GPa and $B'_0 = 5.51$. $E(V)$ curve for γ-Se yields $B_0 = 0.05$ GPa and $B'_0 = 8.08$. Data points correspond to *ab initio* results while solid lines correspond to the fitted Birch-Murnaghan equation of state. The square corresponds to the (V_0, E_0) minimum obtained without pressure. (b) $P(V)$ curves for β- and γ-Se.

distinctive features can help identify the allotropic form of Se using Raman spectroscopy.

This allows us to obtain free energy dependency with respect to temperature, as depicted in Fig. 7. The entropic contribution is more important for β-Se. This may be due to the fact that more degrees of freedom are available for the vibrations of the ions as the rings are roughly free to vibrate independently from one another, whereas the chain structure of γ-Se constrains the vibrations in the c crystallographic axis.

The dependency in temperature and pressure of the ideal structures Gibbs' energies can be extrapolated from the obtained data, following equation (3). The thermal dependency is modeled *via* the simulation of phonons. Expressions of $E(T)$, $S(T)$, and free energy at $P = 0$ $F(T) = E(T) - T \times S(T)$ can be found in Ref. [41] [equations (8), (10), and (11)]. Of course, this is appropriate far below the melting point; near melting point studies would require molecular dynamic simulations.

$$G(P,T) \simeq \underbrace{E(T) - T \times S(T)}_{F(T)(\text{phonons})} + \underbrace{P \left. \frac{\partial E}{\partial P} \right|_{T=0} (P) + P \times V(P)}_{\text{Birch-Murnaghan}}$$

(3)

(a)

(b)
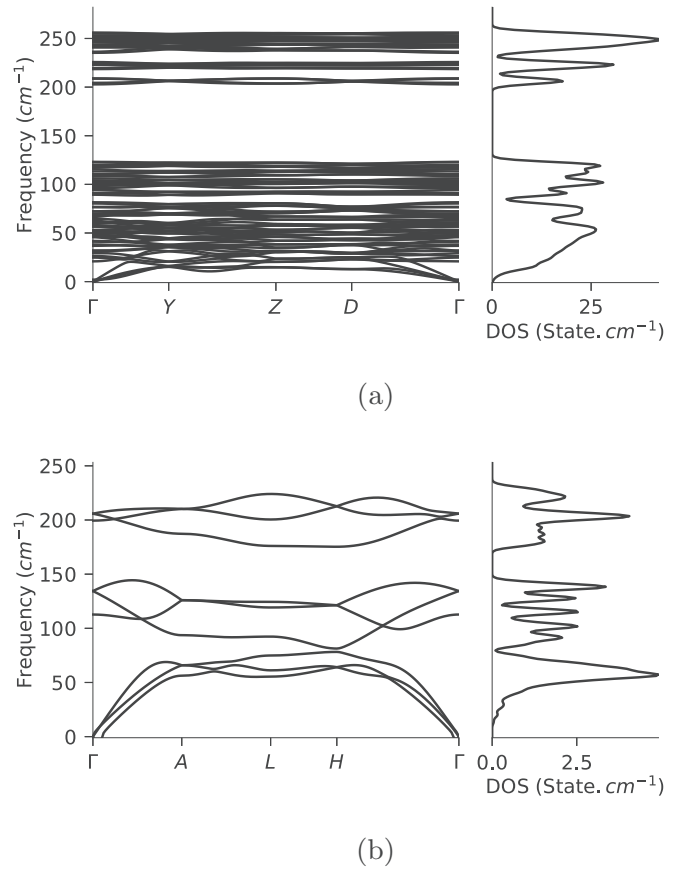
FIG. 6. Phonon band structure and DOS for (a) β-Se [Γ (0,0,0), Y($\frac{1}{2}$,0,0), Z(0,$\frac{1}{2}$,0), D(0,$\frac{1}{2}$,$\frac{1}{2}$)] computed with PBE-GD3-BJ and (b) γ-Se [Γ (0,0,0), A(0,0,$\frac{1}{2}$), L($\frac{1}{2}$, 0, $\frac{1}{2}$), H($\frac{1}{3}$, $\frac{1}{3}$, $\frac{1}{2}$)] computed with PBE-GD3.

The Gibbs' energy difference gives the calculated pressure-temperature phase diagram presented in Fig. 8. The 1D phase γ-Se is the low-temperature phase, as observed experimentally [55]. This is consistent with the fact that thin film synthesis, during which temperature is typically of a few hundreds of degrees, always leads to the formation of γ-Se [6,7]. It should be noted that due to the strong assumptions made to come to such a result, the absolute values of pressure and temperature should be considered with care. Only the studied phases are represented in Fig. 8 (a strong mismatch is
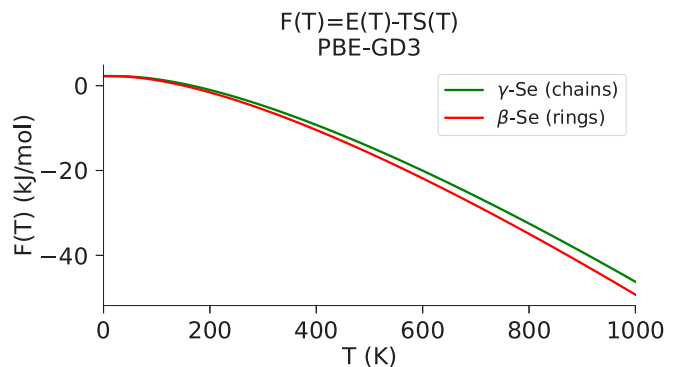
FIG. 7. Free energy of each phase, in kJ/mol, plotted against temperature.
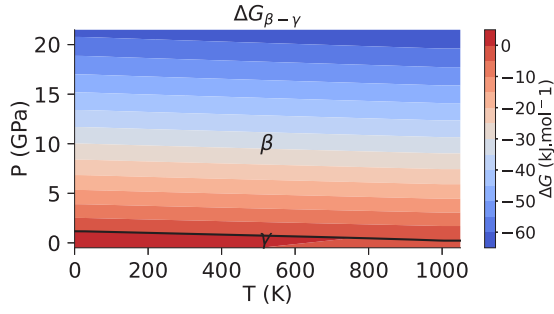
FIG. 8. Calculated phase diagram of crystal selenium against pressure and temperature. $\Delta G_{\beta-\gamma}(T,P) = G_\beta(T,P) - G_\gamma(T,P)$.

observed between theory and experiment in terms of critical P and T at the phase transition but the trend is respected). As mentioned previously, a phase transition towards a monoclinic system is expected at a few dozen GPa, as reported in the experimental literature. However, the exact structure as well as the pressure at which the transition occurs remains a matter of debate.

Note that the entropic contribution to the Gibbs' energy is more important than the volumic term here. It might explain why, counterintuitively, the low-pressure phase γ-Se has a slightly higher density of 4.80 than that of 4.61 of β-Se.

B. Free formation energies of intrinsic interstitial defect of γ-Se, the standard phase of Se

The relative simplicity of the structures offers the opportunity to test the model further and to get closer to the Gibbs' free energy of formation which is rigorously the thermodynamic quantity to aim for. This will allow us to check the validity of the approximation made in the supercell point defect model which consists of ignoring the entropic contribution. In the dilute defect limit, volume change due to the defect is supposed to be zero. Hence, so is the change in

the volumic term of the Gibbs' energy $P \times V$. The free formation energy of formation $\Delta F_f^{D,q}(\mu_{E_F}, T)$ is computed, in order to quantify the error made by ignoring the entropic part. In the following discussion, the notation is simplified to lighten the expressions and T always refers to the crystal growth temperature noted T_{growth} previously. As noted by Freysoldt *et al.* [56], it is rigorously the thermodynamic quantity to calculate. In metals, free energy of defect creation has been calculated for systems such as Al and Cu, taking into account both configurational and vibrational entropies [57,58]. Similar studies in semiconductors remain scarce and limited to well-known materials such as Si, diamond, Ge, and GaN [59,60].

The computation of the configuration entropy requires no additional DFT calculation compared to a standard DFE study but only a refinement of the post-treatment step, while accounting for the most important part of the entropy. Thus, first only the configurational entropy will be taken into account, not the vibrational one. Only the configurational entropy as expressed in equation (4) was taken into account in a first approximation.

$$S_{\text{conf}} = k_B([D^q] - [D^q]\ln[D^q] + [D^q]\ln(N_{\text{sites}})) \quad (4)$$

As expressed in the system of equation (5), the free energy depends on the entropy among other things. In turn, the configurational entropy is a function of the defect concentration, which is a function of the free energy among other things. We chose to describe the defect concentration through a Fermi-Dirac distribution to improve the precision, as the Boltzmann statistic is the limit behavior of the Fermi-Dirac one. This triangular dependency causes a practical difficulty. It can be overcome by solving the first equation of (5) of unknown quantity ΔF using a standard root-finding algorithm. It implies that the fundamental quantity in the model is no more determined in a single step from μ_{E_F} but using a self-consistent loop.

$$\begin{cases} \Delta F_f^{D,q}(\mu_{E_F}, T) = \Delta E_f^{D,q}(\mu_{E_F}) - T S_{\text{conf}}(\Delta F_f^{D,q}) \\ S_{\text{conf}}([D^q]) = k_B([D^q] - [D^q]\ln[D^q] + [D^q]\ln(N_D^{\text{sites}})) \\ [D^q](\Delta F_f^{D,q}) = N_D^{\text{sites}}\left(1 + e^{\frac{\Delta F_f^{D,q}}{k_B T}}\right)^{-1} \end{cases} \quad (5)$$

Equation (4) is applied to Se$_i$ in γ-Se and plotted against volumic defect concentration in Fig. 9(a). Of course, the same line of thoughts can be applied to any defect. Let us keep in mind that the expression of $S_{\text{conf}}([D^q])$ used in equation (5) is obtained by considering the possible configurations of a system containing n defects and N atoms, then by simplifying the obtained expression using the Stirling approximation $\ln N! \simeq N \ln N - N$ and exploiting $\frac{n}{N} \ll 1$. Furthermore, for high defect concentrations, the dilute defect model becomes irrelevant as the system tends to become a solid solution. This is a different problem which should be addressed using an appropriate methodology which differs from the one used in this work. Thus, the model employed here becomes gradually irrelevant as the defect concentration in the system reaches the solid-solution domain. The reasoning here is of

mathematical order. Most of the domains envisioned hereafter are far from reality and considered only to test the limits of the model. Of course, above a defect ratio of 100% represented by the dotted vertical blue line in Fig. 9(a), the model loses any physical meaning. For realistic defect concentrations, the $T \times S$ product is inferior to 0.10 eV for temperatures up to 1250 K. The range of growth temperatures considered (500–1250 K) corresponds to typical temperatures encountered in different growth/deposition processes for elemental selenium. Low temperatures would be employed in vacuum processes such as PVD and high temperatures in ceramic routes. So far, merely by looking at the expression of the configurational entropy used in the model, one can see that in the most extreme limit of 100% defect ratio the $T \times S$ product would weigh no more than 0.10 eV. One would like to go further and

(a)

(b)
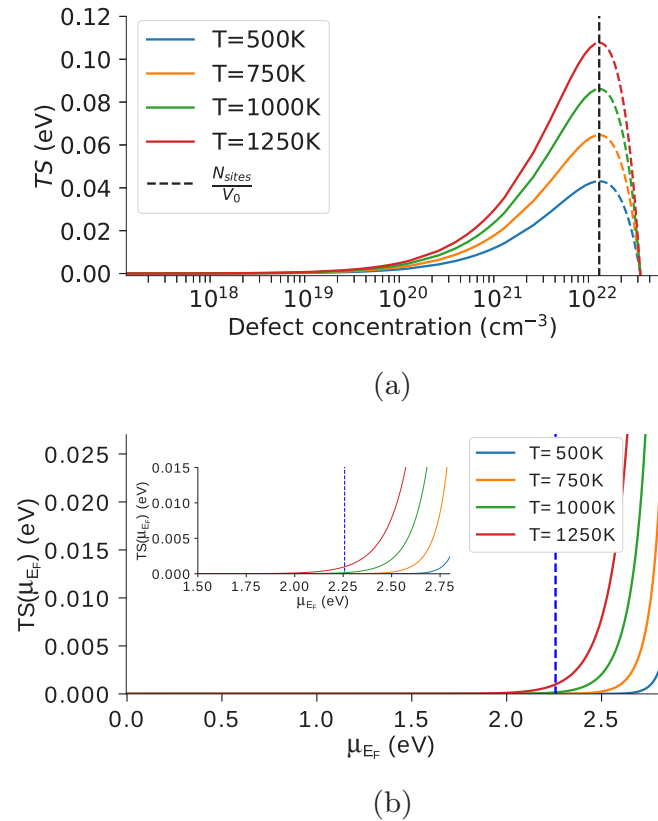
FIG. 9. Se_i in γ-Se $q = -2$. (a) Product of the configurational entropy and crystal growth temperature with respect to defect concentration $TS([D])$ as obtained from the second equation in (5). The blue dotted line stands for $\frac{N_{sites}}{V_0}$, the maximum possible limit for the defect ratio (100% faulted). (b) Product of the configurational entropy and crystal growth temperature with respect to the Fermi level $TS(\mu_{E_F})$ obtained by self-consistently solving the system of equations (5). The encapsulated figure zooms on the vicinity of the CBM to show the scale-up in the high variation region.

estimate the actual dependency of $T \times S$ in Fermi level μ_{E_F} and see whether this value of $\simeq 0.10$ eV is actually met. Note that the very low maximum values for the configurational entropy validate the assumption that the vibrational entropy associated with the defect creation can be safely ignored as $S_{conf} \gg S_{vib}$.

Then, the system of equations (5) is solved self-consistently to obtain the variations of entropy with respect to the position of the Fermi level μ_{E_F}. The weight of the product of the temperature by the configurational entropy $T \times S$ is inferior to 5 meV throughout the band gap, far below the maximum 0.10 eV noticed during the previous analysis of $S([D])$. As the formation enthalpy of Se_i in β-Se, which is the main term of the free energy, decreases with increasing Fermi level, the calculated defect concentration increases with the Fermi level. It leads to an increase in the entropic term. Although it is experimentally known that the real γ-Se material is a p-type one, it is still interesting to look at the range of Fermi level values for which the entropic term would weigh the most. For values of the Fermi level within the band gap, the entropic term is of the order of magnitude of the millielectronvolt or less. The approximation of the free energy by the enthalpy of formation appears thus entirely justified for this defect. It is

only for very high values of μ_{E_F} (unrealistic for a p-type semiconductor) that the DFE of Se_i would become low enough for the entropic term to increase significantly. As a reminder, the crossing point between the VBM and the formation enthalpy of Se_i^{2-} is around 3 eV.

V. CONCLUSION

Ab initio simulations on two allotropic forms of selenium encountered at ambient pressure and temperature were performed. The Birch-Murnaghan equation of state fitted onto a series of ideal models and phonon calculations allowed us to get the contribution to the Gibbs' free energy of pressure and temperature, respectively, for the ideal structures. It shows that the infinite chains of γ-Se are favored over the metastable ring structure β-Se at low pressure and temperature.

Then, intrinsic point defects of both phases were investigated, revealing that β-Se has practically no conductivity while the fair hole conductivity of γ-Se originates from selenium interstitials. Geometric modifications induced by selenium vacancies were studied in detail. It was shown that the ability of the rings to relax to a structure relatively close in terms of environment after the introduction of the vacancy compensates the energy required to break two Se-Se chemical bonds. Comparatively, breaking two such bonds in the chains is easier but results in a very different structure, replacing a covalent bond by a long range interaction, which is not favored energetically. These considerations provide an explanation for the lower V_{Se} DFE in β-Se than in γ-Se despite stronger Se-Se bonds (shorter Se-Se distances).

The problem of counting potential interstitial sites in β-Se was discussed and it was preferred not to calculate the Fermi level in this phase. In γ-Se, such an issue does not appear and the simulations were performed, exhibiting a typical p-type behavior.

Then, antimony and bromine doping were investigated. All proved ineffective in β-Se, whereas antimony was found to improve significantly the hole conductivity in γ-Se *via* the creation of Sb_{Se} substitutional defects. Given these results, one can advise for selenium used in optoelectronic devices to be grown rather at high temperature as long as the γ phase can be maintained and conductivity improved by antimony doping.

Pressure and temperature effects were taken into account for the phase diagram based on the ideal structures. Se_i provided a test case to investigate the impact of configurational entropy. The calculation prove that for selenium, it can be safely neglected. An abacus of configurational entropy values is calculated to provide the quantitative data needed for the decision on the need for the configurational entropy in a defect study.

[1] T. K. Todorov, S. Singh, D. M. Bishop, O. Gunawan, Y. S. Lee, T. S. Gershon, K. W. Brew, P. D. Antunez, and R. Haight, Nat. Commun. **8**, 682 (2017).

[2] W. Smith, Nature (London) **7**, 303 (1873).

[3] C. E. Fritts, Am. J. Sci. **s3-26**, 465 (1883).

[4] T. Nakada and A. Kunioka, Jpn. J. Appl. Phys. **24**, L536 (1985).

[5] J. S. Park, S. Kim, Z. Xie, and A. Walsh, Nat. Rev. Mater. **3**, 194 (2018).

[6] J. Qian, K.-J. Jiang, J.-H. Huang, Q.-S. Liu, L.-M. Yang, and Y. Song, Angew. Chem. Int. Ed. **51**, 10351 (2012).

[7] M. Zhu, F. Hao, L. Ma, T.-B. Song, C. E. Miller, M. R. Wasielewski, X. Li, and M. G. Kanatzidis, ACS Energy Lett. **1**, 469 (2016).

[8] M. Panahi-Kalamuei, M. Salavati-Niasari, and S. M. Hosseinpour-Mashkani, J. Alloys Compd. **617**, 627 (2014).

[9] C. Platzer-Björkman, P. Zabierowski, J. Pettersson, T. Törndahl, and M. Edoff, Prog. Photovolt. **18**, 249 (2010).

[10] Y. Di, Q. Zeng, C. Huang, D. Tang, K. Sun, C. Yan, Y. Wang, S. Ke, L. Jiang, X. Hao, Y. Lai, and F. Liu, Sol. Energy Mater. Sol. Cells **185**, 130 (2018).

[11] S. Chaudhary, A. Umar, and S. Mehta, Prog. Mater. Sci. **83**, 270 (2016).

[12] S. C. Singh, S. K. Mishra, R. K. Srivastava, and R. Gopal, J. Phys. Chem. C **114**, 17374 (2010).

[13] O. Degtyareva, E. Gregoryanz, H. K. Mao, and R. J. Hemley, High Press. Res. **25**, 17 (2005).

[14] L. Properzi, A. Polian, P. Munsch, and A. D. Cicco, High Press. Res. **33**, 35 (2013).

[15] G. Parthasarathy and W. B. Holzapfel, Phys. Rev. B **38**, 10105 (1988).

[16] Y. Akahama, M. Kobayashi, and H. Kawamura, Phys. Rev. B **47**, 20 (1993).

[17] Y. Akahama, M. Kobayashi, and H. Kawamura, Jpn. J. Appl. Phys. **31**, L1621 (1992).

[18] Y. Akahama, M. Kobayashi, and H. Kawamura, Phys. Rev. B **56**, 5027 (1997).

[19] M. Otani and N. Suzuki, Phys. Rev. B **63**, 104516 (2001).

[20] A. K. Bhatnagar, K. V. Reddy, and V. Srivastava, J. Phys. D **18**, L149 (1985).

[21] S. Tutihasi and I. Chen, Phys. Rev. **158**, 623 (1967).

[22] P. Cherin and P. Unger, Acta Cryst. B **28**, 313 (1972).

[23] A. P. Saunders, J. Phys. Chem. **4**, 423 (1900).

[24] A. Maaninen, J. Konu, R. S. Laitinen, T. Chivers, G. Schatte, J. Pietikäinen, and M. Ahlgrén, Inorg. Chem. **40**, 3539 (2001).

[25] J. Knights and E. Davis, Solid State Commun. **11**, 543 (1972).

[26] G. Kresse and J. Hafner, Phys. Rev. B **47**, 558 (1993).

[27] G. Kresse and J. Hafner, Phys. Rev. B **49**, 14251 (1994).

[28] G. Kresse and J. Furthmüller, Comput. Mater. Sci. **6**, 15 (1996).

[29] G. Kresse and J. Furthmüller, Phys. Rev. B **54**, 11169 (1996).

[30] J. P. Perdew, K. Burke, and M. Ernzerhof, Phys. Rev. Lett. **77**, 3865 (1996).

[31] S. Grimme, J. Antony, S. Ehrlich, and H. Krieg, J. Chem. Phys. **132**, 154104 (2010).

[32] S. Grimme, S. Ehrlich, and L. Goerigk, J. Comput. Chem. **32**, 1456 (2011).

[33] A. D. Becke and E. R. Johnson, J. Chem. Phys. **127**, 154108 (2007).

[34] J. Sun, A. Ruzsinszky, and J. P. Perdew, Phys. Rev. Lett. **115**, 036402 (2015).

[35] J. Heyd, G. E. Scuseria, and M. Ernzerhof, J. Chem. Phys. **118**, 8207 (2003).

[36] J. Paier, R. Hirschl, M. Marsman, and G. Kresse, J. Chem. Phys. **122**, 234102 (2005).

[37] See Supplemental Material at http://link.aps.org/supplemental/10.1103/PhysRevB.103.094111 for more information. See SM Table III for β-Se structure parameters calculated using different methodologies compared with experimental data. See SM Table IV for γ-Se structure parameters calculated using different methodologies compared with experimental data. See SM Eq. (1) for the Birch-Murnaghan equation of state. See SM Fig. 1 for the crystallographic structure of γ-Se. See SM Fig. 2 for SCAN electronic band structure and DOS for β- and γ-Se. See SM Fig. 3 for variations of closest-neighbors interatomic distances after the introduction of V_{Se} in β- and γ-Se.

[38] E. Péan, J. Vidal, S. Jobic, and C. Latouche, Chem. Phys. Lett. **671**, 124 (2017).

[39] A. Stoliaroff, S. Jobic, and C. Latouche, J. Comput. Chem. **39**, 2251 (2018).

[40] X. Wu, D. Vanderbilt, and D. R. Hamann, Phys. Rev. B **72**, 035105 (2005).

[41] A. Togo and I. Tanaka, Scr. Mater. **108**, 1 (2015).

[42] A. Stoliaroff, A. Lecomte, O. Rubel, S. Jobic, X. Zhang, C. Latouche, and X. Rocquefelte, ACS Appl. Energy Mater. **3**, 2496 (2020).

[43] A. Stoliaroff, S. Jobic, and C. Latouche, J. Phys. Chem. C **124**, 4363 (2020).

[44] D. Caprion and H. R. Schober, Phys. Rev. B **62**, 3709 (2000).

[45] J. de Lima, T. Grandi, and R. de Biasi, J. Non-Cryst. Solids **286**, 93 (2001).

[46] P. Jóvári, R. G. Delaplane, and L. Pusztai, Phys. Rev. B **67**, 172201 (2003).

[47] M. Marple, J. Badger, I. Hung, Z. Gan, K. Kovnir, and S. Sen, Angew. Chem. Int. Ed. **56**, 9777 (2017).

[48] R. Keller, W. B. Holzapfel, and H. Schulz, Phys. Rev. B **16**, 4404 (1977).

[49] J. Sun, R. C. Remsing, Y. Zhang, Z. Sun, A. Ruzsinszky, H. Peng, Z. Yang, A. Paul, U. Waghmare, X. Wu, M. L. Klein, and J. P. Perdew, Nat. Chem. **8**, 831 (2016).

[50] E. Streltsov, S. Poznyak, and N. Osipovich, J. Electroanal. Chem. **518**, 103 (2002).

[51] W. Waller, *Electronics Design Materials*, Macmillan Engineering Craft Series (Palgrave Macmillan, London, 1971).

[52] A. Stoliaroff, N. Barreau, S. Jobic, and C. Latouche, Theor. Chem. Acc. **137**, 102 (2018).

[53] F. Birch, Phys. Rev. **71**, 809 (1947).

[54] F. Favot and A. Dal Corso, Phys. Rev. B **60**, 11427 (1999).

[55] V. Brazhkin, S. Popova, and R. Voloshin, Phys. B: Condens. Matter **265**, 64 (1999).

[56] C. Freysoldt, B. Grabowski, T. Hickel, J. Neugebauer, G. Kresse, A. Janotti, and C. G. Van de Walle, Rev. Mod. Phys. **86**, 253 (2014).

[57] B. Grabowski, T. Hickel, and J. Neugebauer, Phys. Status Solidi (b) **248**, 1295 (2010).

[58] X. Zhang, B. Grabowski, T. Hickel, and J. Neugebauer, Comput. Mater. Sci. **148**, 249 (2018).

[59] O. K. Al-Mushadani and R. J. Needs, Phys. Rev. B **68**, 235205 (2003).

[60] S. K. Estreicher, M. Sanati, D. West, and F. Ruymgaart, Phys. Rev. B **70**, 125209 (2004).